

Temperature-Dependent Paracrystalline Nucleation in Atomically Disordered Diamonds

ZhongTing Zhang, ZhouYu Fang, HengAn Wu, and YinBo Zhu*



Cite This: *Nano Lett.* 2024, 24, 312–318



Read Online

ACCESS |

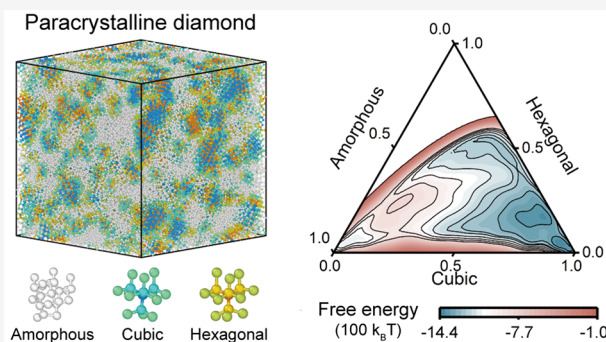
Metrics & More

Article Recommendations

Supporting Information

ABSTRACT: Atomically disordered diamonds with medium-range order realized in recent experiments extend our knowledge of atomic disorder in materials. However, the current understanding of amorphous carbons cannot answer why paracrystalline diamond (p-D) can be formed inherently different from other tetrahedral amorphous carbons (ta-Cs), and the emergence of p-D seems to be easily hindered by inappropriate temperatures. Herein, we performed atomistic-based simulations to shed light on temperature-dependent paracrystalline nucleation in atomically disordered diamonds. Using metadynamics and two carefully designed collective variables, reversible phase transitions among different ta-Cs can be presented under different temperatures, evidenced by corresponding local minima on the free energy surface and reaction path along the free energy gradient. We found that p-D is preferred in a narrow range of temperatures, which is comparable to real experimental temperatures under the Arrhenius framework. The insights and related methods should open up a perspective for investigating other amorphous carbons.

KEYWORDS: *paracrystalline diamonds, atomically disordered diamonds, amorphous carbons, free energy surface*



Carbon has a rich variety of allotropes due to its complex bonding modes (sp , sp^2 , and sp^3), among which a series of highly disordered structures are collectively known as amorphous carbons,^{1–7} including the two-dimensional monolayer and three-dimensional (3D) blocky amorphous structures. While the monolayer carbon phase is dominated by sp^2 bonds,⁶ the 3D amorphous carbons cover wide ranges of density and sp^3 -bond content, possessing diverse and unusual physical and mechanical properties as well as many application prospects in the future.⁸ Benefiting from the development of high-pressure technologies, the existence of tetrahedral amorphous carbons (ta-Cs) has been demonstrated experimentally,^{9–12} labeling sp^3 -rich phases with highly atomistic disordering. Under high-pressure compression, sp^2 -rich glass carbons (GCs) can transform into sp^2 – sp^3 mixed amorphous carbons.^{9,10} Nevertheless, the diamond phase would be formed when GCs were heated at 1200 °C and 25 GPa.¹⁰ By laser heating under high pressure, quenchable amorphous diamond was obtained,¹³ in which the atomic structure was confirmed with nearly complete sp^3 bonding. Recently, Shang et al.¹⁴ and Tang et al.¹⁵ coincidentally reported atomically disordered diamonds with a sp^3 concentration close to 100%. The synergistic control of high-pressure and high-temperature (HPHT) conditions in their experiments revealed that atomically disordered diamonds can be obtained only within a narrow temperature range.^{14,15} Starting from precursors of C_{60} , the structural evolution of atomically disordered diamonds

by sp^2 to sp^3 hybridization and the corresponding pressure–temperature dependence were reported through simulations.^{15,16} With an adiabatic-bias MD technique,¹⁷ Tang et al. also obtained p-D with paracrystalline fraction up to 70%,¹⁵ successfully bridging the temporal gap between the experiment and simulation. However, the temperature effect on the formation of sp^3 -rich amorphous carbons is still ambiguous, further impeding us to fundamentally understand why atomically disordered sp^3 -hybridized carbons can be formed unexpectedly and how to obtain them under suitable HPHT conditions.

Although atomically disordered diamonds reported by Shang et al. and Tang et al. are not the same,^{14,15} medium-/short-range order was evidenced inherently by X-ray diffraction patterns and high-resolution transmission electron microscopy images.^{11,14,15,18,19} Diamond-like nuclei with the characteristic size of ~1 nm were clearly highlighted within the disordered matrix, manifesting severely distorted crystal lattices and unconventional crystal-plane-like stripes.^{11,14,15} Tang et al.

Received: October 19, 2023

Revised: December 19, 2023

Accepted: December 19, 2023

Published: December 22, 2023



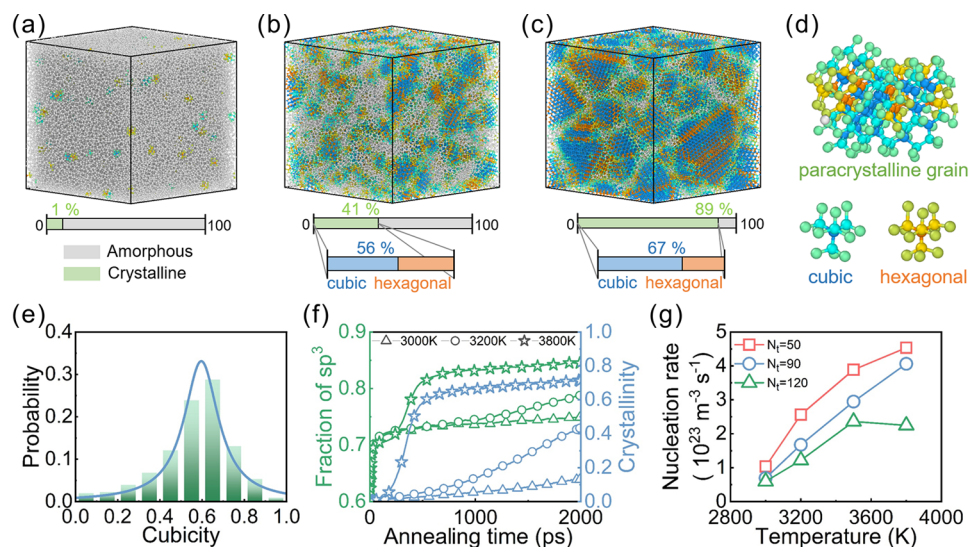


Figure 1. Three typical ta-Cs obtained from HPHT annealing simulations. (a–c) Snapshots of a-D, p-D, and NPD, respectively. Each model contains 108,000 atoms. (d) Representative paracrystallite in p-D. In paracrystallites, CD and HD atoms are stacked in a disordered manner. (e) Probability distribution of cubicity in p-D, fitted by a Lorentz distribution. (f) Evolutions of sp^3 fraction and crystallinity at different annealing temperatures. (g) Nucleation rates calculated by the YM method.

defined their samples as the paracrystalline diamond (p-D), while unsuitable HPHT conditions would result in the formation of amorphous diamond (a-D) or nanopolycrystalline diamond (NPD).^{13–15,20,21} It is reminiscent of heterogeneous nucleation in solid matter. Within a narrow temperature region, the further crystal growth was prevented, and heterogeneous nucleation was suspended suddenly, resulting in paracrystallites randomly embedded into an amorphous matrix without the long-range order.^{11,14,15} Thus, a question arises in atomically disordered diamonds of what the temperature effect on the paracrystalline nucleation is. In this Letter, we performed large-scale molecular dynamics (MD) simulations and well-tempered metadynamics (METAD) by also combining it with integrated tempering sampling (METAITS) simulations to unveil the mystery of nucleation in p-D. The free energy surface and reaction path were calculated to understand why p-D can be formed distinctly different from a-D and NPD and how temperature controls the nucleation and growth of paracrystallites in an amorphous matrix.

In the first series of MD simulations, a-D, p-D, and NPD were obtained under annealing temperatures of 3000, 3200, and 3800 K, respectively. Based on the Arrhenius framework proposed by Marks and co-workers,²² the temperatures simulated with environment-dependent interatomic potential (EDIP)²³ can approximately correspond to real temperatures ranging from 1300 to 1800 K, close to the synthesis temperatures reported by Shang et al. (1143~1373 K) and Tang et al. (1200~1600 K).^{14,15} Marks and co-workers have demonstrated that in large-scale MD simulations the EDIP potential can well simulate the topological microstructures of amorphous carbons and provides good all-around performance.^{22,24,25} Specifically, at high densities like 3.0 g/cc, the EDIP force field showed outstanding abilities to predict correct amorphous microstructures with the highest sp^3 fractions (>55%) compared with other empirical potentials.²⁴ As illustrated in Figure 1(a–c), carbon atoms within the amorphous, cubic-diamond (CD), and hexagonal-diamond (HD) states are clearly identified to highlight the difference

among three phases. It is obvious that p-D exhibits medium-range order,^{14,15} originating from the nanometer-sized paracrystallites that are composed of CD and HD nanonuclei in a highly disordered stacking manner (Figure 1d). To define the cubicity of p-D, paracrystallites of >20 atoms are counted for the calculation of the proportion of CD atoms. Figure 1e shows that the cubicity of p-D follows the Lorentz distribution in which the peak value of ~0.6 reveals more CD atoms than HD atoms in paracrystallites. Thus, CD configurations can be formed more easily (Figure S1). Under different annealing temperatures, the sp^3 fraction and crystallinity as functions of annealing time plotted in Figure 1f indicate the nucleation events in a-D, p-D, and NPD are quite different. The sp^3 fraction and crystallinity both tend to flatten out at 3000 and 3800 K, indicating the sufficient structural stability of the prepared samples. For the temperature of 3200 K, the two curves rise slowly and steadily, representing the continuous nucleation and growth of paracrystallites. Prolonging the annealing time would increase the degree of paracrystallization, and higher temperatures would result in the transformation from paracrystallites to large-sized diamond grains. It is also found that the nucleation of paracrystallites and diamond grains prefers to happen where the first-neighbor four layers of carbon atomic shells (cutoff within 3.5 Å) contain more than 24 neighboring atoms (Figure S2).

To calculate the nucleation rates under different temperatures, the Yasuoka and Matsumoto (YM) method was used,²⁶ where the number of grains larger than a predefined threshold (N_t) is monitored during simulations. The size and number of paracrystallites were counted through the DBSCAN cluster method (Figure S3). Usually, N_t is related to the critical nucleation size,²⁶ but its exact value is unknown.¹⁵ We thus selected N_t ranging from 30 to 120 to analyze the influence of temperature on the nucleation rate. The number of nucleation sites was counted by considering different N_t and temperatures (Figure S4). It can be deduced that higher temperatures can result in the arising of more nucleation sites and higher nucleation rates (Figure 1g), whereas it is still confusing how temperature influences the nucleation and growth of para-

crystallites. Traditional MD simulations cannot answer in p-D why paracrystallites can exist stably in an amorphous matrix.

We then used well-tempered METAD^{27–30} and METAITS^{31–33} simulations to calculate the free energy surface, further exploring the temperature effect on the nucleation. METAD and METAITS simulations are popular enhanced sampling methods to accelerate simulation system evolution and construct the free energy surface that controls spontaneous phase transitions.^{27,29,34} The essence is that the addition of Gaussian bias potential energy can force the system to escape from free energy local minima.^{28,29,34} In general, this method highly depends on the appropriately defined collective variables (CVs), which are low-dimensional coordinates used to accurately describe related phase transitions.³⁵ In previous studies, several series of CVs have shown to be effective.^{36–41} Tang et al. used the mean value of the Steinhardt order parameter as CVs to perform adiabatic-bias MD simulations.¹⁵ The benchmark of selected CVs is to accurately and effectively distinguish different microstructural topologies during the nucleation and crystallization.^{27,29,35} On the consideration of paracrystallites embedded into an amorphous matrix, the construction of effective CVs for p-D requires an in-depth analysis of microstructural topology.

Subsequently, the structure factor ($S(Q)$), radial distribution function ($G(r)$), and order parameters are used to highlight the difference in microstructural topology. Figure 2a plots $S(Q)$

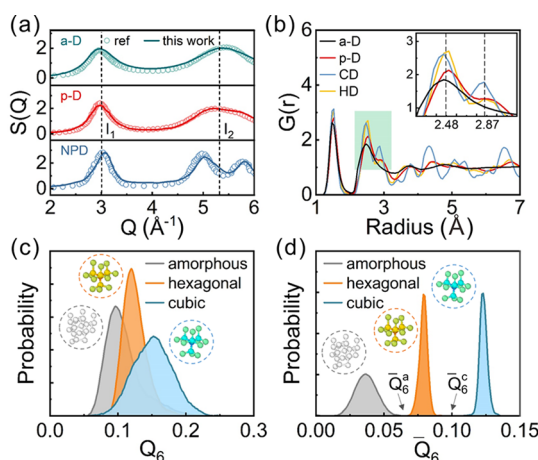


Figure 2. Structural analysis. (a) Structural factor ($S(Q)$). The experimental data are extracted from ref 15. Copyright 2021 Springer Nature. (b) Radial distribution function $G(r)$. The structures used to calculate $G(r)$ were selected from MD trajectories. The inset highlights the difference among different phases at the locations of the second and third peaks in $G(r)$ curves. (c) Distributions of the sixth Steinhardt order parameter (Q_6). (d) Distributions of the local-averaged sixth Steinhardt order parameter (\bar{Q}_6).

curves of a-D, p-D, and NPD, where our simulations are in line with recent experiments,¹⁵ indicating the structural reliability of the samples using the EDIP potential in our simulations. The difference between I_1 and I_2 peaks in $S(Q)$ s is usually used to distinguish a-D and p-D.¹⁵ Figure 2b shows $G(r)$ curves for a-D, p-D, CD, and HD, respectively, where the front three peaks represent the first-neighbor three layers of atomic shells. The sixth Steinhardt order parameter (Q_6)⁴² distributions plotted in Figure 2c demonstrate that they are overlapped for carbon atoms in the amorphous, CD, and HD states, while the inset in Figure 2b indicates that there are distinct differences in

the first-neighbor three layers of atomic structures. Therefore, we averaged Q_6 within the first-neighbor three layers (<3.2 Å) to obtain the local-averaged order parameter \bar{Q}_6 .⁴³ As illustrated in Figure 2d, the \bar{Q}_6 distributions can well distinguish carbon atoms within the three states. We thus used \bar{Q}_6 to construct effective CVs for free energy calculations. Herein, the numbers of CD and HD atoms in simulated structures are marked as N_C and N_H , respectively, which are computed as follows:

$$\left\{ \begin{array}{l} N_C = \sum_{i=1}^N (1 - \sigma(\bar{Q}_6^i, \bar{Q}_6^c)) \\ N_H = N - N_C - \sum_{i=1}^N \sigma(\bar{Q}_6^i, \bar{Q}_6^a) \end{array} \right.$$

where N is the total number of carbon atoms in simulation box; \bar{Q}_6^c and \bar{Q}_6^a are two critical thresholds between different atomic structures, and $\sigma(x, x_0) = [1 - (x/x_0)^6]/[1 - (x/x_0)^{12}]$ is a switching function that approximately equals to 0 when $x > x_0$ and equals to 1 elsewhere. In Figure 2d, $\bar{Q}_6^c = 0.1$ and $\bar{Q}_6^a = 0.068$ can be obtained. Then, the proportions of CD and HD atoms ($S_C = N_C/N$ and $S_H = N_H/N$) are selected as new CVs for METAD and METAITS simulations in the next.

It is interesting to observe continuous and reversible transformations among several typical steady and metastable phases in METAD simulations at 3600 K and 20 GPa. Figure 3a plots the atomic structures of five phases, corresponding to local minima marked on the free energy surface (Figure 3b,c). The local minimum point of p-D in Figure 3b is inconspicuous due to the high annealing temperature. Free energy surfaces under other temperatures were also calculated (Figure S6). In Figure 3d, evolutions of S_C and S_H indicate that the system experiences phase transitions from a-D to p-D, NPD, CD, and finally HD, pushed by the addition of Gaussian bias potential energy in simulations. Here, the HD state is an unstable hexagonal-rich phase, since S_H never goes beyond 0.6 throughout the simulation. The continuous and reversible fluctuations of S_C and S_H imply that the system undergoes violent reversible phase transitions, and the calculated free energy surface can be considered to be converged.^{28,29} The validity of our proposed CVs is verified by free energy local minima and reversible phase transitions. The spontaneous solid-to-solid phase transition from a-D to p-D was also found in classical annealing simulations under 3500 K (Figure S7), indicating that the emergence of paracrystallites in the amorphous matrix can be activated by a suitable range of high temperatures. However, one METAD can only calculate the free energy surface under a preset temperature, resulting in that studying the temperature effect requires many time-consuming simulations.^{28,29} Since the degree of convergence is uncontrollable in different METAD simulations, free energy surfaces under different temperatures are difficult to unify, and there may be large randomness in comparisons.

To further explore the effect of temperature on nucleation, METAITS simulations were carried out using the proposed CVs. The better sampling efficiency and faster convergence rate of METAITS enable it to directly reweigh free energy surfaces considering different temperatures within one simulation.³³ Five (meta)stable phases obtained from METAITS simulations are shown in Figure 4a. Small-grained and

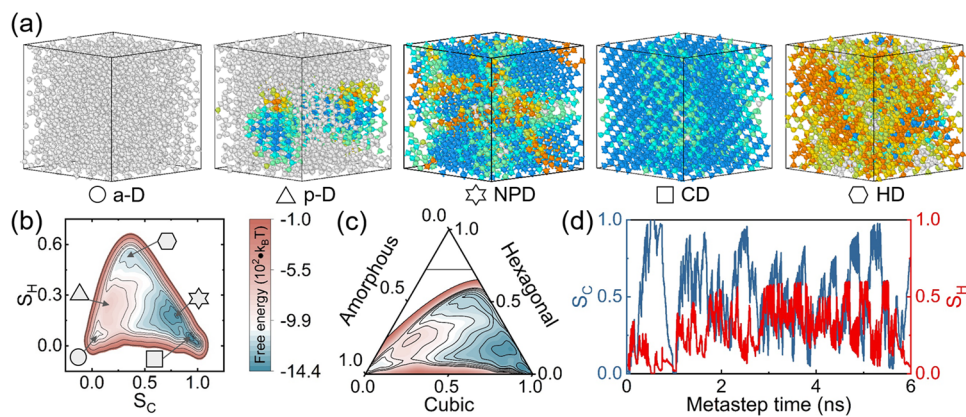


Figure 3. Well-tempered METAD simulations using two carefully designed CVs (S_C and S_H). (a) Typical snapshots of steady and metastable structures obtained from METAD. These phases are labeled by different symbols. (b) Free energy surface in the plane of S_C versus S_H . (c) Free energy surface normalized by proportions of amorphous, CD, and HD atoms. (d) S_C and S_H as a function of metastep time.

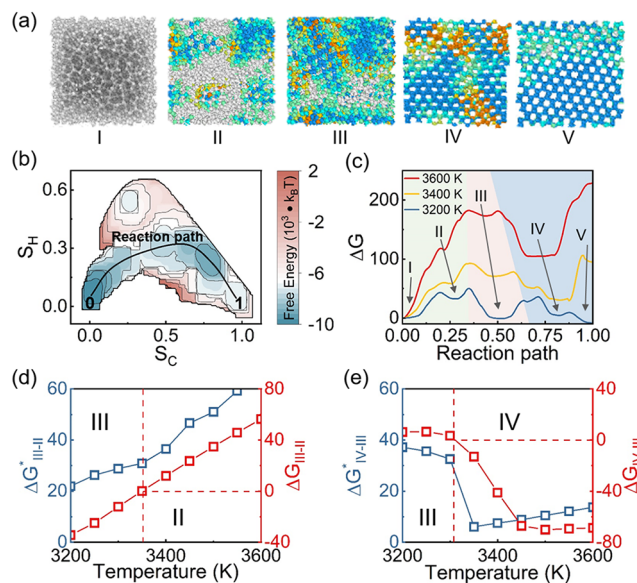


Figure 4. Temperature dependence of nucleation simulated using METAITS. (a) Typical snapshots of different phases along a reaction path; namely, a-D (I), small-grained p-D (II), large-grained p-D (III), NPD (IV), and CD (V), respectively. (b) Free energy surface calculated from METAITS. Five phases in (a) are, respectively, located at the local lowest points in (b). The reaction path is plotted along the free energy gradient. (c) The change of free energy along the reaction path under different annealing temperatures. (d) Phase transition from small-grained to large-grained p-D. (e) Phase transition from p-D to NPD. In (d) and (e), the blue and red lines with symbols denote the free energy barrier (ΔG^*) and free energy difference (ΔG), respectively. The critical temperature at $\Delta G = 0$ is marked by the crossover point of dashed lines.

large-grained p-D phases can be well distinguished. Most carbon atoms in the small-grained p-D are amorphous, while large-grained p-D possesses a large degree of crystallinity with the disorderly oriented paracrystallites that lack long-range order. The transformation from p-D to NPD can be achieved through the fusion of paracrystallites and the rearrangement of crystal lattice orientations. Figure 4b plots a free energy surface reweighted at 3300 K, in which a reaction path is highlighted along the free energy gradient, ranging from 0 to 1. The changes in free energy along the reaction path under 3200, 3400, and 3600 K are shown in Figure 4c, where five different

primary local minima can be observed, corresponding to the five phases. In comparison to METAD, the free energy calculated here can cover a relatively wide temperature range.³³

In general, the growth of paracrystallites and the rearrangement of carbon lattice orientations are the two most important steps in controlling the synthesis of p-D, in which the former determines the degree of crystallinity and the latter controls whether the synthesized samples can be stabilized in the p-D phase instead of transforming into NPD.¹⁵ The two steps are both spontaneous processes controlled by the free energy surface,⁴⁴ which is obviously affected by temperature. Figure 4d,e shows the free energy barrier ΔG^* and free energy difference ΔG from 3200 to 3600 K for the two important phase transition processes. Based on the Arrhenius framework,²² the temperature range (3200~3600 K) considered in our simulations can approximately correspond to real temperatures from 1300 to 1600 K, which are very close to the synthesis temperatures of atomically disordered diamonds with the medium-range order reported by Shang et al. (1143~1373 K)¹⁴ and Tang et al. (1200~1600 K).¹⁵ In Figure 4d, ΔG^* and ΔG rise steadily with the increase in the annealing temperature. The critical temperature at $\Delta G = 0$ is ~3350 K (corresponding to a real temperature of ~1450 K) for the transformation from small-grained to large-grained p-D phases. In Figure 4e, for the transformation from p-D to NPD, ΔG^* and ΔG decrease very slightly at first but drop sharply when the temperature is larger than the critical value of ~3300 K (corresponding to a real temperature of ~1400 K).

Under a relatively low temperature (<3300 K), Figure 4c indicates that both small-grained and large-grained p-D phases possess sufficiently distinct local minima in the free energy surface. ΔG becomes smaller with the decrease in temperature (Figure 4d). Given that only ΔG is considered, it can be deduced that large-grained p-D with a lower free energy minimum should be more stable and easier to emerge than small-grained p-D.⁴⁴ However, previous simulations and experiments of Tang et al. have yielded different results;¹⁵ that is, the decrease in temperature would lead to the decrease in grain size and crystallization degree.^{14,15} Usually, free energy mainly affects the direction of reactions, while final products also depend strongly on reaction rate.⁴⁴ We thus attribute this mismatch to the decrease in atomic mobility⁴⁵ and thermal fluctuations⁴⁴ under low temperatures, and the consequent decrease in reaction rate results in the appearance of small

paracrystalline embryos being slow and rare, further limiting the growth of these small crystal nuclei. In this case, the crystalline degree and paracrystalline size can be increased by extending the annealing time and raising the annealing temperature suitably.^{14,15} In recent experiments, though both the samples synthesized by Shang et al. and Tang et al. exhibit medium-range order,^{14,15} diamond-like nanograins in the former specimens are smaller and less than that in the latter.^{11,14,15} From the perspective of the free energy analysis, we argue that this difference originates from the temperature effect.

With the increase of temperature, the free energy of both small-grained and large-grained p-D phases rises and their corresponding local minima begin to vanish when the temperature is beyond 3400 K (Figure 4c). This is due to the increasingly violent atomic mobility and thermal fluctuations that destabilize paracrystallites and severely distorted crystal lattices. On the contrary, as the temperature rises (>3300 K), ΔG drops sharply (Figure 4e), and free energy minima of NPD become deeper and deeper (Figure 4c). Thus, under higher temperatures, NPD is more likely to form and stabilize than p-D.¹⁴ This phenomenon is consistent with the samples prepared under 1800 K,¹⁵ whose diffraction peaks correspond exactly to characteristic Bragg peaks of NPD instead of p-D.¹⁵ As expected, when the temperature ranges from ~3200 to 3400 K (corresponding to a real temperature of 1300~1500 K approximately), ta-C is more inclined to stabilize in a p-D phase with medium-range order.^{14,15} With higher temperature, the paracrystallites grow larger. Once the temperature goes beyond a critical value (~3600 K), the synthesized samples tend to transform and stabilize in a long-range order NPD state.¹⁵ It is clear that our simulations and analyses have good mutual verification with the experimental results. It is also anticipated that in the future more powerful force fields (e.g., machine learning potential) for amorphous carbons can be developed to explore the rich surprising properties and phase transitions of noncrystalline carbons.

In summary, we investigated the temperature effect on the nucleation in p-D to answer why p-D can be formed distinctly different from a-D and NPD and how temperature controls the nucleation and growth of paracrystallites in an amorphous matrix. Our large-scale MD simulations and nucleation rate calculated using the YM method revealed that temperature plays a pivotal role in controlling phase transitions of high-density ta-Cs. To unveil the temperature effect, well-tempered METAD and METAITS simulations were carried out based on two CVs constructed by local-averaged sixth-order Steinhardt order parameters. Reversible phase transitions among different (meta)stable phases were realized in simulations and confirmed by the corresponding local minima on the free energy surface and reaction paths along the free energy gradient. We found that when the annealing temperature ranges from ~3200 to 3400 K ta-C is more inclined to stabilize in a p-D phase. Under the Arrhenius framework,²² the critical temperature range of the formation of p-D in simulations has a good mutual verification with real temperatures reported in recent experiments.^{14,15} Our findings should provide theoretical support for the experimental preparation of p-D and open up a new perspective for studying phase transitions of other amorphous carbons.^{9–13,46–50}

■ ASSOCIATED CONTENT

SI Supporting Information

The Supporting Information is available free of charge at <https://pubs.acs.org/doi/10.1021/acs.nanolett.3c04037>.

The details of MD annealing simulations, brief descriptions of the YM method and DBSCAN method, formulas to calculate order parameters and structure factor, and examples for configuring CVs and metadynamics simulations (METAD and METAITS) used in PLUMED patched with LAMMPS. Calculations of nucleation rates (Figures S1–S4), XRD patterns (Figure S5), free energy surfaces (Figure S6), and the solid-to-solid phase transition from a-D to p-D (Figure S7) (PDF)

■ AUTHOR INFORMATION

Corresponding Author

YinBo Zhu – CAS Key Laboratory of Mechanical Behavior and Design of Materials, Department of Modern Mechanics, University of Science and Technology of China, Hefei 230027, China;  orcid.org/0000-0001-9204-9300; Email: zhuyinbo@ustc.edu.cn

Authors

ZhongTing Zhang – CAS Key Laboratory of Mechanical Behavior and Design of Materials, Department of Modern Mechanics, University of Science and Technology of China, Hefei 230027, China

ZhouYu Fang – CAS Key Laboratory of Mechanical Behavior and Design of Materials, Department of Modern Mechanics, University of Science and Technology of China, Hefei 230027, China

HengAn Wu – CAS Key Laboratory of Mechanical Behavior and Design of Materials, Department of Modern Mechanics, University of Science and Technology of China, Hefei 230027, China; State Key Laboratory of Nonlinear Mechanics, Institute of Mechanics, Chinese Academy of Science, Beijing 100190, China;  orcid.org/0000-0003-0288-1617

Complete contact information is available at: <https://pubs.acs.org/10.1021/acs.nanolett.3c04037>

Author Contributions

Z.T. Zhang and Z.Y. Fang contributed equally to this work. Y.B. Zhu conceived the idea and designed the research. H.A. Wu and Y.B. Zhu supervised the project. Z.T. Zhang, Z.Y. Fang, and Y.B. Zhu performed simulations. Y.B. Zhu and Z.T. Zhang analyzed data and wrote the paper.

Notes

The authors declare no competing financial interest.

■ ACKNOWLEDGMENTS

We thank Prof. Nigel A. Marks at Curtin University for providing the EDIP force file. This work was jointly supported by the Youth Innovation Promotion Association CAS (2022465), the National Natural Science Foundation of China (12232016 and 12172346), the Fundamental Research Funds for the Central Universities (WK2090000049), and the Open Fund of Key Laboratory for Intelligent Nano Materials and Devices of the Ministry of Education NJ2022002 (INMD-2022M04). The numerical calculations have been done on the

supercomputing system in the Supercomputing Center of University of Science and Technology of China.

■ REFERENCES

- (1) Marks, N. A.; McKenzie, D. R.; Pailthorpe, B. A.; Bernasconi, M.; Parrinello, M. Microscopic Structure of Tetrahedral Amorphous Carbon. *Phys. Rev. Lett.* **1996**, *76*, 768–771.
- (2) Galli, G.; Martin, R. M.; Car, R.; Parrinello, M. Structural and Electronic Properties of Amorphous Carbon. *Phys. Rev. Lett.* **1989**, *62*, 555–558.
- (3) McKenzie, D. R.; Muller, D.; Pailthorpe, B. A. Compressive-Stress-induced Formation of Thin-Film Tetrahedral Amorphous Carbon. *Phys. Rev. Lett.* **1991**, *67*, 773–776.
- (4) Zhu, Y.; Wang, Y.; Wu, B.; He, Z.; Xia, J.; Wu, H. Micromechanical Landscape of Three-Dimensional Disordered Graphene Networks. *Nano Lett.* **2021**, *21*, 8401–8408.
- (5) Joo, W. J.; Lee, J. H.; Jang, Y.; Kang, S. G.; Kwon, Y. N.; Chung, J.; Lee, S.; Kim, C.; Kim, T. H.; Yang, C. W.; et al. Realization of Continuous Zachariasen Carbon Monolayer. *Sci. Adv.* **2017**, *3*, 2375–2548.
- (6) Toh, C. T.; Zhang, H. J.; Lin, J. H.; Mayorov, A. S.; Wang, Y. P.; Orofeo, C. M.; Ferry, D. B.; Andersen, H.; Kakenov, N.; Guo, Z. L.; et al. Synthesis and Properties of Free-Standing Monolayer Amorphous Carbon. *Nature* **2020**, *577*, 199–203.
- (7) El-Machachi, Z.; Wilson, M.; Deringer, V. L. Exploring the Configurational Space of Amorphous Graphene with Machine-Learned Atomic Energies. *Chem. Sci.* **2022**, *13*, 13720–13731.
- (8) Gogotsi, Y. Not just graphene: The Wonderful World of Carbon and Related Nanomaterials. *MRS Bull.* **2015**, *40*, 1110–1121.
- (9) Lin, Y.; Zhang, L.; Mao, H. K.; Chow, P.; Xiao, Y.; Baldini, M.; Shu, J.; Mao, W. L. Amorphous Diamond: A High-Pressure Superhard Carbon Allotrope. *Phys. Rev. Lett.* **2011**, *107*, No. 175504.
- (10) Hu, M.; He, J.; Zhao, Z.; Strobel, T. A.; Hu, W.; Yu, D.; Sun, H.; Liu, L.; Li, Z.; Ma, M.; et al. Compressed Glassy Carbon: An Ultrastrong and Elastic Interpenetrating Graphene Network. *Sci. Adv.* **2017**, *3*, No. e1603213.
- (11) San-Miguel, A. How to Make Macroscale Non-Crystalline Diamonds. *Nature* **2021**, *599*, 563–564.
- (12) Zhang, S.; Li, Z.; Luo, K.; He, J.; Gao, Y.; Soldatov, A. V.; Benavides, V.; Shi, K.; Nie, A.; Zhang, B.; et al. Discovery of Carbon-based Strongest and Hardest Amorphous material. *Natl. Sci. Rev.* **2022**, *9*, No. nwab140.
- (13) Zeng, Z.; Yang, L.; Zeng, Q.; Lou, H.; Sheng, H.; Wen, J.; Miller, D. J.; Meng, Y.; Yang, W.; Mao, W. L.; Mao, H.-k.; et al. Synthesis of Quenchable Amorphous Diamond. *Nat. Commun.* **2017**, *8*, 322.
- (14) Shang, Y.; Liu, Z.; Dong, J.; Yao, M.; Yang, Z.; Li, Q.; Zhai, C.; Shen, F.; Hou, X.; Wang, L.; et al. Ultrahard Bulk Amorphous Carbon from Collapsed Fullerene. *Nature* **2021**, *599*, 599–604.
- (15) Tang, H.; Yuan, X.; Cheng, Y.; Fei, H.; Liu, F.; Liang, T.; Zeng, Z.; Ishii, T.; Wang, M. S.; Katsura, T.; et al. Synthesis of Paracrystalline Diamond. *Nature* **2021**, *599*, 605–610.
- (16) Ni, K.; Pan, F.; Zhu, Y. Structural Evolution of C60 Molecular Crystal Predicted by Neural Network Potential. *Adv. Funct. Mater.* **2022**, *32*, No. 2203894.
- (17) Marchi, M.; Ballone, P. Adiabatic Bias Molecular Dynamics: A method to Navigate the Conformational Space of Complex Molecular Systems. *J. Chem. Phys.* **1999**, *110*, 3697–3702.
- (18) Elliott, S. R. Medium-Range Structural Order in Covalent Amorphous Solids. *Nature* **1991**, *354*, 445–452.
- (19) Sheng, H. W.; Luo, W. K.; Alamgir, F. M.; Bai, J. M.; Ma, E. Atomic Packing and Short-to-Medium-Range Order in Metallic Glasses. *Nature* **2006**, *439*, 419–425.
- (20) Sumiya, H.; Irfune, T. Hardness and Deformation Microstructures of Nano-Polycrystalline Diamonds Synthesized from Various Carbons under High Pressure and High Temperature. *J. Mater. Res.* **2007**, *22*, 2345–2351.
- (21) Robertson, J. Diamond-like Amorphous Carbon. *Mater. Sci. Eng. R Rep.* **2002**, *37*, 129–281.
- (22) de Tomas, C.; Suarez-Martinez, I.; Vallejos-Burgos, F.; López, M. J.; Kaneko, K.; Marks, N. A. Structural Prediction of Graphitization and Porosity in Carbide-Derived Carbons. *Carbon* **2017**, *119*, 1–9.
- (23) Marks, N. A. Generalizing the Environment-Dependent Interaction Potential for Carbon. *Phys. Rev. B* **2000**, *63*, No. 035401.
- (24) de Tomas, C.; Suarez-Martinez, I.; Marks, N. A. Graphitization of Amorphous Carbons: A Comparative Study of Interatomic Potentials. *Carbon* **2016**, *109*, 681–693.
- (25) de Tomas, C.; Aghajamali, A.; Jones, J. L.; Lim, D. J.; López, M. J.; Suarez-Martinez, I.; Marks, N. A. Transferability in Interatomic Potentials for Carbon. *Carbon* **2019**, *155*, 624–634.
- (26) Yasuoka, K.; Matsumoto, M. Molecular Dynamics of Homogeneous Nucleation in the Vapor Phase. I. Lennard-Jones Fluid. *J. Chem. Phys.* **1998**, *109*, 8451–8462.
- (27) Barducci, A.; Bussi, G.; Parrinello, M. Well-Tempered Metadynamics: A Smoothly Converging and Tunable Free-Energy Method. *Phys. Rev. Lett.* **2008**, *100*, No. 020603.
- (28) Laio, A.; Parrinello, M. Escaping Free-Energy Minima. *Proc. Natl. Acad. Sci. U.S.A.* **2002**, *99*, 12562–12566.
- (29) Laio, A.; Gervasio, F. L. Metadynamics: A Method to Simulate Rare Events and Reconstruct the Free Energy in Biophysics, Chemistry and Material Science. *Rep. Prog. Phys.* **2008**, *71*, No. 126601.
- (30) Tiwary, P.; Parrinello, M. A Time-Independent Free Energy Estimator for Metadynamics. *J. Phys. Chem. B* **2015**, *119*, 736–742.
- (31) Gao, Y. Q. Self-Adaptive Enhanced Sampling in the Energy and Trajectory Spaces: Accelerated Thermodynamics and Kinetic Calculations. *J. Chem. Phys.* **2008**, *128*, No. 134111.
- (32) Gao, Y. Q. An Integrate-Over-Temperature Approach for Enhanced Sampling. *J. Chem. Phys.* **2008**, *128*, No. 064105.
- (33) Yang, Y. I.; Niu, H.; Parrinello, M. Combining Metadynamics and Integrated Tempering Sampling. *J. Phys. Chem. Lett.* **2018**, *9*, 6426–6430.
- (34) Invernizzi, M.; Parrinello, M. Rethinking Metadynamics: From Bias Potentials to Probability Distributions. *J. Phys. Chem. Lett.* **2020**, *11*, 2731–2736.
- (35) Fiorin, G.; Klein, M. L.; Henin, J. Using Collective Variables to Drive Molecular Dynamics Simulations. *Mol. Phys.* **2013**, *111*, 3345–3362.
- (36) Piaggi, P. M.; Valsson, O.; Parrinello, M. Enhancing Entropy and Enthalpy Fluctuations to Drive Crystallization in Atomistic Simulations. *Phys. Rev. Lett.* **2017**, *119*, No. 015701.
- (37) Bonati, L.; Parrinello, M. Silicon Liquid Structure and Crystal Nucleation from ab initio Deep Metadynamics. *Phys. Rev. Lett.* **2018**, *121*, No. 265701.
- (38) Niu, H.; Piaggi, P. M.; Invernizzi, M.; Parrinello, M. Molecular Dynamics Simulations of Liquid Silica Crystallization. *Proc. Natl. Acad. Sci. U.S.A.* **2018**, *115*, 5348–5352.
- (39) Niu, H.; Yang, Y. I.; Parrinello, M. Temperature Dependence of Homogeneous Nucleation in Ice. *Phys. Rev. Lett.* **2019**, *122*, No. 245501.
- (40) Niu, H.; Bonati, L.; Piaggi, P. M.; Parrinello, M. Ab initio Phase Diagram and Nucleation of Gallium. *Nat. Commun.* **2020**, *11*, 2654.
- (41) Li, M.; Zhang, J.; Niu, H.; Lei, Y. K.; Han, X.; Yang, L.; Ye, Z.; Yang, Y. I.; Gao, Y. Q. Phase Transition between Crystalline Variants of Ordinary Ice. *J. Phys. Chem. Lett.* **2022**, *13*, 8601–8606.
- (42) Steinhardt, P. J.; Nelson, D. R.; Ronchetti, M. Bond-Orientational Order in Liquids and Glasses. *Phys. Rev. B* **1983**, *28*, 784–805.
- (43) Lechner, W.; Dellago, C. Accurate Determination of Crystal Structures based on Averaged Local Bond Order Parameters. *J. Chem. Phys.* **2008**, *129*, No. 114707.
- (44) Sosso, G. C.; Chen, J.; Cox, S. J.; Fitzner, M.; Pedevilla, P.; Zen, A.; Michaelides, A. Crystal Nucleation in Liquids: Open Questions and Future Challenges in Molecular Dynamics Simulations. *Chem. Rev.* **2016**, *116*, 7078–7116.
- (45) Zhang, P.; Maldonis, J. J.; Liu, Z.; Schroers, J.; Voyles, P. M. Spatially Heterogeneous Dynamics in a Metallic Glass forming Liquid

Imaged by Electron Correlation Microscopy. *Nat. Commun.* **2018**, *9*, 1129.

(46) Zhang, X.; Zhong, L.; Mateos, A.; Kudo, A.; Vyatskikh, A.; Gao, H. J.; Greer, J. R.; Li, X. Y. Theoretical Strength and Rubber-like Behaviour in Micro-Sized Pyrolytic Carbon. *Nat. Nanotechnol.* **2019**, *14*, 762–769.

(47) Martin, J. W.; Fogg, J. L.; Francas, G. R.; Putman, K. J.; Turner, E. P.; Suarez-Martinez, I.; Marks, N. A. Graphite Rapidly Forms via Annihilation of Screw Dislocations. *Carbon* **2023**, *215*, No. 118386.

(48) Chen, M. W.; Zhu, Y. B.; Xia, J.; Wu, H. A. Molecular Insights into the Initial Formation of Pyrolytic Carbon upon Carbon Fiber Surface. *Carbon* **2019**, *148*, 307–316.

(49) Chen, M. W.; Wu, B.; Zhou, L. C.; Zhu, Y. B.; Wu, H. A. Micromechanical Properties of Pyrolytic Carbon with Interlayer Crosslink. *Carbon* **2020**, *159*, 549–560.

(50) Li, Z.; Wang, Y.; Ma, M.; Ma, H.; Hu, W.; Zhang, X.; Zhuge, Z.; Zhang, S.; Luo, K.; Gao, Y.; et al. Ultrastrong Conductive *in situ* Composite Composed of Nanodiamond Incoherently Embedded in Disordered Multilayer Graphene. *Nat. Mater.* **2023**, *22*, 42–49.